The Gaussian Discriminant Variational Autoencoder (GdVAE): A Self-Explainable Model with Counterfactual Explanations

Supplementary Material

Table of Contents

The Supplement is structured as follows:

- Limitations and societal impacts are discussed in Appendix A.
- In Appendix B, you can find the ELBO derivation (Eqs. (7) and (8)), as well as proofs for the EM-based approach (Algorithm 1) and the optimality of linear explainer functions (Eq. (10)).
- Detailed information about the models used, the training process, and experimental specifics, such as compute resources, hyperparameters, dataset, and asset details, can be found in Appendix C.
- Appendix D delves into the metrics employed for predictive performance analysis and CF quality assessment.
- Additional results related to hyperparameter tuning, trade-off between consistency and realism (Figs. 9 and 10) as well as supplementary qualitative results are presented in Appendix E.

A Limitations and Societal Impacts

A.1 Limitations

We acknowledge several limitations concerning the GdVAE and the evaluation methodology:

- Our datasets for quantitative evaluation were selected to balance computational efficiency, alignment with previous studies, and adherence to the Reproducibility Checklist, emphasizing the provision of central tendency and variation (e.g., mean, standard deviation). Unlike prior CF research, our focus on analyzing both central tendency and variability has led to experiments that are four times more costly (see Appendix C.4). By doing so, we acknowledge the limitations imposed by our dataset selection criteria, yet we argue that these limitations are counterbalanced by the gains in the reproducibility of our experimental results.
- Our method, unlike [30] and [14], enables simultaneous manipulation of all class-related attributes but lacks fine-grained control over individual image attributes. Incorporating multiple prototypes, as in [13], could enhance GdVAE's predictive performance and capability to manipulate individual image attributes.

- Our quantitative evaluation of CF methods is currently limited to binary classification problems, and future evaluations of multi-class problems are needed to advance CF literature. Unfortunately, most visual CF methods (Tab. 1) evaluate CFs for binary tasks like CelebA, where attributes are not mutually exclusive. Those that use multi-class settings do not scale well to a high number of classes without modification, requiring the training of a model for each binary CF class pair [26, 40]. Other approaches require time-consuming inference-time optimization [24, 30] or an additional image of the CF class to guide CF generation [16, 47]. Our method can be expanded to multiple classes. For multiple classes, our CFs (Eq. (10)) can be generated without changes by choosing a reference class. Ambiguity between logits and softmax makes user interaction less convenient, yet setting $\delta < 0$ achieves CFs inducing class flips. Results for MNIST and CIFAR, presented in Figs. 15 and 16, demonstrate CFs for the simpler consistency task by swapping the logits of the predicted and counterfactual classes. This strategy is effective for high-confidence class predictions, such as with MNIST, though it formally only changes the class without necessarily switching to the specified CF class.
- Our approach utilizes a class-conditional encoder model $q_\phi(z|x, y)$. Significantly reduced computational costs can be achieved by employing unconditional models, such as $q_\phi(z|x)$. In [12], a clustering solution is presented, directly leveraging unconditional encoder and decoder models. However, further analyses are needed to conclude the performance implications.
- The EM-based method described in Algorithm 1 is an integral part of the error backpropagation process. Consequently, using a high number of iterations results in very deep computational graphs, which can introduce challenges, including issues like vanishing gradients and other forms of instability.
- All our experiments employ relatively simple network architectures, and we strive to maintain uniform training configurations as closely as possible. For instance, our baselines share the same backbone architecture, are trained with loss functions as faithful as feasible to the original implementations, and undergo training for a duration of 24 epochs. These limitations may result in methods like EBPE performing below their full potential, considering that in their original versions, both EBPE and its extension, DISSECT, were trained for 300 epochs. Results after additional training epochs are in Tab. 12.

A.2 Societal Impacts

Our GdVAE is not inherently associated with specific applications that directly cause negative societal impacts. However, it does possess the potential for misuse in unethical ways. For instance, given our generative models, there exists the possibility of their modified use for generating deep fake images with altered attributes. Furthermore, although our SEM provides insights into the model, it does not guarantee the detection of all fairness issues, existing biases, or results that align with attribution-based explanations. Our methods complement existing fairness ([33]) and explainability ([34, 35]) enhancement techniques rather than replacing them.

B Proofs

B.1 Variational Lower Bound of the Joint Log-Likelihood

In this section, we derive the Evidence Lower Bound (ELBO) for our main paper's loss function, which is represented by Eqs. (7) and (8). We define the key variables as follows with x representing the input data (e.g., an image), y corresponding to the target class, and z representing our latent variables. The general ELBO for the model is derived by

$$\begin{aligned}
\log p_\theta(x,y) &= \log \int p_\theta(x,y,z)dz = \log \int p_\theta(x,y,z)\frac{q_\phi(z|x,y)}{q_\phi(z|x,y)}dz \\
&= \log \mathbb{E}_{q_\phi(z|x,y)}\left[\frac{p_\theta(x,y,z)}{q_\phi(z|x,y)}\right] \\
&\geq \mathbb{E}_{q_\phi(z|x,y)}\left[\log \frac{p_\theta(x,y,z)}{q_\phi(z|x,y)}\right] (ELBO) \\
&= \mathbb{E}_{q_\phi(\cdot)}[\log p_\theta(x,y,z)] - \mathbb{E}_{q_\phi(\cdot)}[\log q_\phi(z|x,y)] \\
&= \mathbb{E}_{q_\phi(\cdot)}[\log p_\theta(x|y,z)] + \mathbb{E}_{q_\phi(\cdot)}[\log p_\theta(y,z)] - \mathbb{E}_{q_\phi(\cdot)}[\log q_\phi(z|x,y)] \\
&= -\mathcal{L}^{M1,2}(\theta,\phi;x,y),
\end{aligned}$$

with $q_\phi(\cdot) = q_\phi(z|x,y)$. The loss function for the first model M1 including a CVAE with an additional class prior $p_\theta(y,z) = p_\theta(z|y)p_\theta(y)$ is given by

$$\begin{aligned}
\mathcal{L}^{M1} &= -\mathbb{E}_{q_\phi(\cdot)}[\log p_\theta(x|y,z)] - \mathbb{E}_{q_\phi(\cdot)}[\log p_\theta(y,z)] + \mathbb{E}_{q_\phi(\cdot)}[\log q_\phi(z|x,y)] \\
&= -\mathbb{E}_{q_\phi(\cdot)}[\log p_\theta(x|y,z)] - \mathbb{E}_{q_\phi(\cdot)}[\log p_\theta(z|y)] \\
&\quad - \mathbb{E}_{q_\phi(\cdot)}[\log p_\theta(y)] + \mathbb{E}_{q_\phi(\cdot)}[\log q_\phi(z|x,y)] \\
&= -\mathbb{E}_{q_\phi(\cdot)}[\log p_\theta(x|y,z)] + KL(q_\phi(z|x,y)||p_\theta(z|y)) - \log p_\theta(y).
\end{aligned}$$

The loss for the second model M2 with a classifier and latent prior $p_\theta(y,z) = p_\theta(y|z)p_\theta(z)$ is given by

$$\begin{aligned}
\mathcal{L}^{M2} &= -\mathbb{E}_{q_\phi(\cdot)}[\log p_\theta(x|y,z)] - \mathbb{E}_{q_\phi(\cdot)}[\log p_\theta(y,z)] + \mathbb{E}_{q_\phi(\cdot)}[\log q_\phi(z|x,y)] \\
&= -\mathbb{E}_{q_\phi(\cdot)}[\log p_\theta(x|y,z)] - \mathbb{E}_{q_\phi(\cdot)}[\log p_\theta(y|z)] \\
&\quad - \mathbb{E}_{q_\phi(\cdot)}[\log p_\theta(z)] + \mathbb{E}_{q_\phi(\cdot)}[\log q_\phi(z|x,y)] \\
&= -\mathbb{E}_{q_\phi(\cdot)}[\log p_\theta(x|y,z)] + KL(q_\phi(z|x,y)||p_\theta(z)) - \mathbb{E}_{q_\phi(\cdot)}[\log p_\theta(y|z)]\,.
\end{aligned}$$

The loss function $\tilde{\mathcal{L}}^{gd} = \tilde{\mathcal{L}}^{gd}(\theta,\phi;x,y)$ for a joint training of the conditional variational autoencoder and classifier can be obtained by combining $\mathcal{L}^{M1} = \mathcal{L}^{M1}(\theta,\phi;x,y)$ and $\mathcal{L}^{M2} = \mathcal{L}^{M2}(\theta,\phi;x,y)$. We then obtain

$$\begin{aligned}
\tilde{\mathcal{L}}^{gd} =& \alpha\mathcal{L}^{M1} + \beta\mathcal{L}^{M2} \\
=& -(\alpha+\beta)\mathbb{E}_{q_\phi(\cdot)}[\log p_\theta(x|y,z)] + \alpha\left(KL(q_\phi(z|x,y)||p_\theta(z|y)) - \log p_\theta(y)\right) \\
&+ \beta\left(KL(q_\phi(z|x,y)||p_\theta(z)) - \mathbb{E}_{q_\phi(\cdot)}[\log p_\theta(y|z)]\right),
\end{aligned} \tag{12}$$

with $q_\phi(\cdot) = q_\phi(z|x,y)$.

B.2 Variational Expectation Maximization for the Marginalization Process (Algorithm 1)

In this section, we employ variational expectation maximization (EM) to provide a proof for the iterative algorithm, as depicted in Algorithm 1. This algorithm serves as a fundamental component for marginalization. It's worth noting that this EM process is nested within the overarching variational optimization of the GdVAE. Consequently, we switch the roles of distributions, with $p(\cdot)$ representing the variational distribution and $q(\cdot)$ signifying the model distribution.

Consider the variable pair (x, z, y) within the model distribution $q_\phi(x, z, y)$, where only x is observable. The objective of variational EM is to optimize the model parameters ϕ by maximizing the marginal likelihood $q_\phi(x)$. This optimization is achieved by leveraging a lower bound on the marginal likelihood, using the 'variational' distribution $p_\theta(z, y|x)$. This lower bound is defined by

$$\begin{aligned}\log q_\phi(x) &\geq \mathbb{E}_{p_\theta(z,y|x)}[\log q_\phi(x,z,y)] \quad - \mathbb{E}_{p_\theta(z,y|x)}[\log p_\theta(z,y|x)] \\ &= -\mathbb{E}_{p_\theta(z,y|x)}\left[\log \frac{p_\theta(z,y|x)}{q_\phi(z,y|x)}\right] + \log q_\phi(x).\end{aligned}$$

By rearranging the lower bound, we obtain the function $\mathcal{J}(p, \phi)$, which serves as the objective for the EM algorithm. This function is meant to be maximized and is defined by

$$\begin{aligned}\Rightarrow 0 \geq \mathcal{J}(p,\phi) &= -KL(p_\theta(z,y|x)||q_\phi(z,y|x)) \\ &= -\mathbb{E}_{p_\theta(z,y|x)}\left[\log \frac{p_\theta(z,y|x)}{q_\phi(z,y|x)}\right] = -\mathbb{E}_{p_\theta(z,y|x)}\left[\log \frac{p(y|z)p_\theta(z|x)}{q_\phi(y|x)q_\phi(z|x)}\right].\end{aligned}$$

We further assume conditional independence and apply the following factorizations $q_\phi(z, y|x) = q_\phi(y|z, x)q_\phi(z|x) = q_\phi(y|x)q_\phi(z|x)$, with $q_\phi(z|x) = \sum_{y=1}^{K} q(z|x, y)q_\phi(y|x)$. Likewise, we define $p_\theta(z, y|x) = p(y|z)p_\theta(z|x)$. The parameters θ and ϕ were omitted for the distributions assumed to remain constant throughout the EM procedure. These distributions include $p(y|z)$, representing the classifier employing the prior encoder, and $q(z|x, y)$, representing the recognition model of the GdVAE. The iterative EM procedure for step $t \in \{1, \ldots, T\}$ can be expressed as follows:

E-Step: Choose a distribution $p{=}p_\theta(z, y|x)$ that maximizes $\mathcal{J}(p, \phi)$ for fixed ϕ^t.

- Since $p(y|z)$ is fixed the optimum is given by choosing $p_\theta(z|x) = q_{\phi^t}(z|x)$.

M-Step: Choose parameters ϕ^{t+1} that maximize $\mathcal{J}(p, \phi)$ for fixed $p{=}p_\theta(z, y|x)$.

- The optimum is given by choosing $q_{\phi^{t+1}}(y|x) = \mathbb{E}_{q_{\phi^t}(z|x)}[p(y|z)]$. This choice defines $q_{\phi^{t+1}}(z|x) = \sum_{y=1}^{K} q(z|x, y)q_{\phi^{t+1}}(y|x)$ as well.

Proof for the M-Step: We can simplify the optimization process by assuming that both $q_\phi(z|x)$ and $p_\theta(z|x)$ are Gaussian mixture models with the same number, denoted as K, of mixture components. Drawing inspiration from [10], we can next

derive a lower bound, denoted as $\mathcal{L}(p,\phi)$, for $\mathcal{J}(p,\phi)$ through the application of the *log-sum* inequality and by inserting $p_\theta(z|x) = q_{\phi^t}(z|x)$ into $\mathcal{J}(p,\phi)$

$$\begin{aligned}\mathcal{J}(p,\phi) &= -\int \sum_{y=1}^{K} p(y|z) q_{\phi^t}(z|x) \cdot \log \frac{p(y|z)\sum_{y^\star=1}^{K} q(z|x,y^\star) q_{\phi^t}(y^\star|x)}{q_\phi(y|x)\sum_{y^\star=1}^{K} q(z|x,y^\star) q_\phi(y^\star|x)} dz \\ &\geq \mathcal{L}(p,\phi) = -\int \sum_{y=1}^{K} p(y|z) q_{\phi^t}(z|x) \cdot \log \frac{p(y|z) q(z|x,y) q_{\phi^t}(y|x)}{q_\phi(y|x) q(z|x,y) q_\phi(y|x)} dz \\ &= -\mathbb{E}_{q_{\phi^t}(z|x)}\left[\sum_{y=1}^{K} p(y|z) \log \frac{p(y|z) q_{\phi^t}(y|x)}{q_\phi(y|x) q_\phi(y|x)}\right].\end{aligned}$$

To maximize $\mathcal{L}(p,\phi)$, we employ the Lagrange multiplier $\lambda \in \mathbb{R}$ and set the derivative with respect to a specific class c to zero

$$\begin{aligned}0 &= \frac{\partial}{\partial q_\phi(c|x)}\left[\mathcal{L}(p,\phi) - \lambda(\sum_{y=1}^{K} q_\phi(y|x) - 1)\right] = \mathbb{E}_{q_{\phi^t}(z|x)}\left[2\frac{p(c|z)}{q_\phi(c|x)}\right] - \lambda, \\ &\Rightarrow q_{\phi^{t+1}}(y|x) = \mathbb{E}_{q_{\phi^t}(z|x)}[p(y|z)]\,.\end{aligned}$$

We determine the value of λ by solving this equation for K classes, incorporating the property $\sum_{y=1}^{K} q_\phi(y|x) = 1$. Subsequently, we arrive at the solution $q_{\phi^{t+1}}(y|x) = \mathbb{E}_{q_{\phi^t}(z|x)}[p(y|z)]$ or, equivalently, the parameter ϕ^{t+1} that maximizes $\mathcal{J}(p,\phi)$ while keeping $p_\theta(z,y|x)$ fixed. This optimization is performed for a single input x, and we approximate the expectation through Monte Carlo integration. Therefore, we sample $z^{(s)}$ from $q_{\phi^t}(z|x)$ and calculate $q_{\phi^{t+1}}(y|x) = \mathbb{E}_{q_{\phi^t}(z|x)}[p(y|z)] \approx \frac{1}{S}\sum_{s=1}^{S} p_\theta(y|z^{(s)})$.

B.3 Optimality of Linear Explainer Functions (Eq. (9) and Eq. (10))

Euclidean Space ($V := I$). Our SEM is regularized to produce a linear separating hyperplane due to the linear classifier we employ. This results in a linear path for CF generation, where the classifier's gradient vector w describes the *shortest path* for CF generation (see Fig. 4a). This *latent space closeness* is also used as an L2-based metric $\text{dist}_I^2(z^{(1)}, z^{(2)})$ to measure CF proximity [43] or to directly optimize a perceptual loss for CF generation [24].

Riemannian Manifolds ($V := \Sigma_z^{-1}$). A generalized perspective on the distance function arises from considering the theoretical analysis on Riemannian manifolds presented in [5,19]. According to [19], a Riemannian manifold, denoted as the pair $(\mathcal{M}, v_z)$, can be understood as a smoothly curved space $\mathcal{M}$ (*e.g.*, latent space) equipped with a Riemannian metric v_z. The Riemannian metric is an inner product $v_z(a,b) = \langle a,b\rangle_z = a^T V(z) b$ on the tangent space $\mathcal{T}_z\mathcal{M}$ for each $z \in \mathcal{M}$. The metric tensor $V(z)$ is a positive definite matrix that induces a distance measure. Assuming a constant metric tensor or single metric learning,

the Mahalanobis distance is obtained [5, 19]

$$\mathrm{dist}_V^2\left(z^{(1)}, z^{(2)}\right) = \left\|z^{(1)} - z^{(2)}\right\|_V^2 = \left(z^{(1)} - z^{(2)}\right)^T V \left(z^{(1)} - z^{(2)}\right). \quad (13)$$

If the metric tensor is chosen to be the identity matrix $V := I$, we obtain the L2-based Euclidean distance. To define a smooth continuous Riemannian metric with a metric tensor in every point z, [19] propose

$$V(z) = \sum_{k=1}^{K} \pi_k(z) V_k, \quad (14)$$

where V_k are pre-trained metric tensors, *e.g.*, obtained by a Large Margin Nearest Neighbor classifier, which are associated with the mean of each class. π_k are weights that change smoothly with z, where each $\pi_k > 0$ and $\sum_{k=1}^{K} \pi_k = 1$. As an example of a smooth weight function, they use the following

$$\pi_k(z) \propto \exp\left(-\frac{\rho}{2}\left\|z - z^{(k)}\right\|_{V_k}^2\right), \quad (15)$$

with the constant ρ and class means $z^{(k)}$. Based on this continuous Riemannian metric (see Eq. (14)), [5] propose using the trained covariance matrices from a VAE's encoder $q_\phi(z|x) = \mathcal{N}\left(\mu_z(x;\phi), \Sigma_z(x;\phi)\right)$ to define the metric. Specifically, they employ a weighted linear combination of $V_k = \Sigma_z^{-1}(x^{(k)};\phi)$, where the training data, or a subset thereof, is used to approximate the metric in the latent space. In addition to Eq. (14), there is a supplementary additive component which is approximately zero. They further observe that, due to the Evidence Lower Bound (ELBO) objective, variables that are close in the latent space with respect to $V(z)$ will also produce samples that are close in the image space in terms of L2 distance, which is crucial for ensuring counterfactual proximity.

Optimization and Assumptions. In our analysis, we assume that the regularizer included in the ELBO induces a surrogate posterior $q_\phi(z|x, y)$ that closely approximates the true posterior $p_\theta(z|y) = \mathcal{N}\left(\mu_z(y;\theta), \Sigma_z(y;\theta)\right)$. Given this approximation, we may consider using pre-trained metric tensors from the GDA (Gaussian discriminant analysis) classifier instead of those derived from a Large Margin Nearest Neighbor classifier [19]. By doing so, as referenced in Eq. (14), we obtain a Riemannian metric

$$V(z) = \sum_{k=1}^{K} \pi_k(z) \Sigma_z^{-1}(y = k;\theta), \quad (16)$$

with $\pi_k(z) = p_\theta(y = k|z)$. In our experiments, we use only two classes and have chosen the covariance to be independent of the class y in order to obtain linear discriminants. Consequently, this results in a constant metric tensor, effectively employing a single metric

$$V(z) = \pi_1(z)\Sigma_z^{-1} + (1 - \pi_1(z))\Sigma_z^{-1} = \Sigma_z^{-1} = V. \quad (17)$$

Having defined two types of distance metrics, the L2 and Mahalanobis distances, we can now optimize the objective

$$\mathcal{I}_f(z,\delta) = \arg\min_{z^\delta} \text{dist}_V^2(z^\delta, z), \quad \text{subject to } f(z^\delta) = \delta. \tag{18}$$

To minimize the objective $\text{dist}_V^2(z^\delta, z)$, we use a Lagrange multiplier $\lambda \in \mathbb{R}$ and set the derivatives with respect to the counterfactual z^δ and λ to zero

$$\mathcal{L}(z^\delta) = \left(z^\delta - z\right)^T V \left(z^\delta - z\right) + \lambda(f(z^\delta) - \delta), \tag{19}$$

$$\frac{\partial \mathcal{L}(z^\delta)}{\partial z^\delta} = 2\left(z^\delta - z\right) V + \lambda w = 0, \quad \Rightarrow z^\delta = z + \frac{\lambda}{2} V^{-1} w, \tag{20}$$

$$\frac{\partial \mathcal{L}(z^\delta)}{\partial \lambda} = 0, \quad \Rightarrow f(z^\delta) = w^T z^\delta + b = \delta. \tag{21}$$

By combining Eqs. (20) and (21), we arrive at the solution

$$w^T z^\delta = w^T z + \frac{\lambda}{2} w^T V^{-1} w = \delta - b, \tag{22}$$

$$\Rightarrow z^\delta = z + \kappa V^{-1} w, \text{ with } \kappa = \frac{\delta - w^T z - b}{w^T V^{-1} w}. \tag{23}$$

Given the assumptions used, we obtain a linear explainer function to generate counterfactuals, regardless of whether we choose the common L2-based metric $V = I$ (Euclidean space) or the Riemannian metric $V = \Sigma_z^{-1}$. Training with $\Sigma_z = \sigma^2 I$ instead of $\Sigma_z = \text{diag}\left(\sigma_{z_1}^2, ., \sigma_{z_M}^2\right)$ results in equivalent explainer functions, thus yielding equal empirical results for both L2-based and Riemannian-based metrics. Consequently, a linear function is optimal, and thus there is no superior solution for generating counterfactuals under these conditions. If the assumption that $q_\phi(z|x,y) \approx p_\theta(z|y)$ is not met, a non-linear CF method (*e.g.*, C3LT) may better fulfill the proximity property in the image space.

C Training and Model Details

The software to train and perform inference with our GdVAE model is available in the supplemental code.

C.1 Datasets

MNIST [31]. The MNIST dataset comprises two sets: a training set with 60,000 labeled examples and a test set with 10,000 labeled examples. Each example is a 28x28 pixel grayscale image representing a handwritten digit ranging from 0 to 9. For the predictive performance analysis (Tab. 2) we use all classes and for the evaluation of counterfactuals (Tab. 3) we exclusively utilize the digits 0 and 1 for the training and to generate counterfactuals (denoted by "MNIST-Binary 0/1"). We adhere to the standard data splits for both training and testing.
CIFAR-10 [29]. The CIFAR-10 dataset comprises over 60,000 images, along with annotations for ten classes. Each example is a 32x32 pixel image with 3 color channels. We adhere to the standard data splits for both training and testing. This dataset is used to analyze the predictive performance in Tab. 2.
CelebA [32]. The CelebA dataset comprises over 200,000 face images, along with annotations that cover a range of attributes, including gender, age, and facial expression. In our analysis, we employ a center crop of 128x128 pixels for the images and resize them to 64x64 pixel images with 3 color channels. For counterfactual evaluation (Tab. 3), we use the attributes of "smiling" (labeled as 1) and "not smiling" (labeled as 0), while the "gender" attribute is used to assess predictive performance (Tab. 2). We adhere to the standard data splits for both training and testing. For licensing details and information on human subject data collection, please see the reference [32].
FFHQ [25]. The Flickr-Faces-HQ (FFHQ) dataset comprises over 70,000 high-resolution (1024x1024 pixels) images of human faces, curated for diversity in age, ethnicity, and accessories. The dataset was developed by NVIDIA. For counterfactual generation (Fig. 1), we use the attributes of "smiling" (labeled as 1) and "not smiling" (labeled as 0) available at https://github.com/DCGM/ffhq-features-dataset/. For licensing details and information on human subject data collection, please see the reference [25].

C.2 GdVAE Details

GdVAE Training. The training algorithm is outlined in the supplemental code. The fundamental GdVAE training procedure, does not include the consistency loss. This particular training method is employed in Tab. 2 and in Tab. 3 the consistency regularizer is incorporated. During the training process, we employ both the global and local-L2 explainer functions to generate counterfactual (CF) examples. To generate samples, we follow a random selection procedure, sampling from either explainer function with equal probability. Fig. 5 illustrates the inputs to the loss functions.

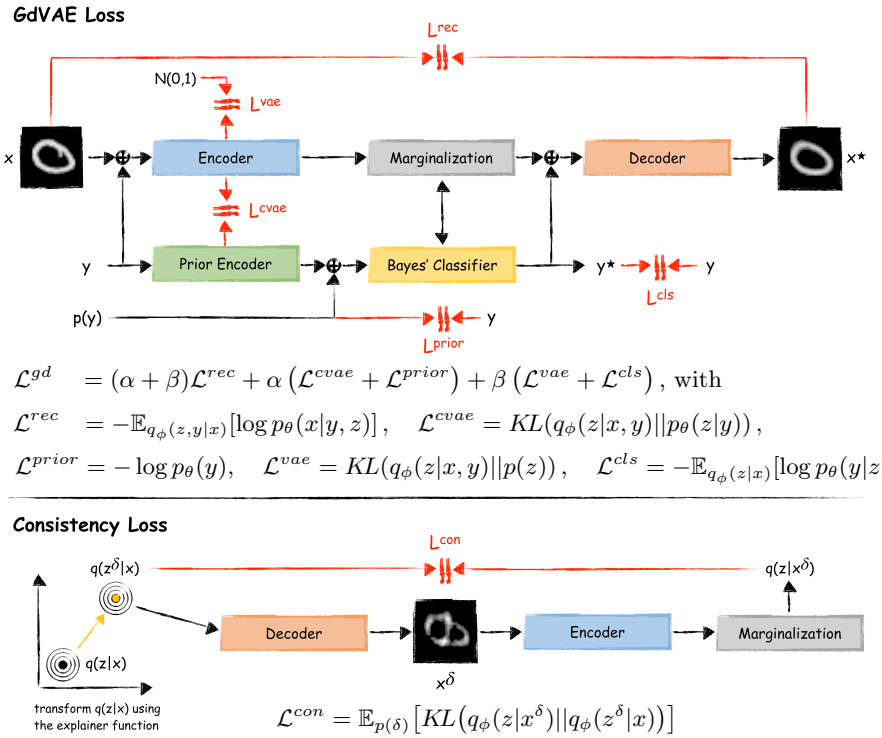

$$\mathcal{L}^{gd} = (\alpha+\beta)\mathcal{L}^{rec} + \alpha\left(\mathcal{L}^{cvae} + \mathcal{L}^{prior}\right) + \beta\left(\mathcal{L}^{vae} + \mathcal{L}^{cls}\right), \text{ with}$$

$$\mathcal{L}^{rec} = -\mathbb{E}_{q_\phi(z,y|x)}[\log p_\theta(x|y,z)], \quad \mathcal{L}^{cvae} = KL(q_\phi(z|x,y)||p_\theta(z|y)),$$

$$\mathcal{L}^{prior} = -\log p_\theta(y), \quad \mathcal{L}^{vae} = KL(q_\phi(z|x,y)||p(z)), \quad \mathcal{L}^{cls} = -\mathbb{E}_{q_\phi(z|x)}[\log p_\theta(y|z)].$$

$$\mathcal{L}^{con} = \mathbb{E}_{p(\delta)}\left[KL\left(q_\phi(z|x^\delta)||q_\phi(z^\delta|x)\right)\right]$$

Fig. 5: Diagram illustrating the GdVAE model components and their interactions, highlighting the key elements that contribute to loss function computation.

The hyperparameters used for training and architectural decisions to replicate the results from the paper are summarized in Tab. 5. The architectures are presented in Tabs. 6 to 10. We maintain consistent hyperparameters ($\alpha/\beta = 1$, $\gamma = 1$, $T = 3$, $S = 20$) across all datasets. Baseline models adopt dataset-specific settings for improved results, as indicated in Tab. 12.

GdVAE Architectures. The architecture of the neural network for the CelebA GdVAE is inspired by the encoder and decoder configurations presented in [9]. When dealing with CelebA, we use 4×4 kernels for every convolutional layer, with a stride of 2 and padding set to 1. However, the last convolutional layer deviates from this pattern and employs the default stride of 1 with no padding. In between these layers, Rectified Linear Units (ReLU) are applied.

For more detailed model specifications related to CelebA, please consult Tab. 7. The notation "FC ($\times$2)" signifies that two distinct fully connected networks are in use for both the mean and log variance calculations. In our architecture, "Conv2d" stands for 2D convolution, while "ConvT2d" corresponds to 2D transposed convolution. The stride and padding settings for these operations are represented as "s" and "p", respectively. These operations are implemented using the torch.nn package in PyTorch.

It's worth noting that the prior encoder and label embeddings remain consistent across all models and datasets, as displayed in Tab. 6. Architectural details for other datasets are provided in Tabs. 8 to 10. For FFHQ we use the pre-trained StyleGAN architecture based on [53]. Our GdVAE model, as shown in Table 10, is integrated between StyleGAN's encoder and decoder. For a comprehensive understanding of the hyperparameters used in the experiments, please refer to Tab. 5 in the case of experiments detailed in Tabs. 2 and 3. An ablation study regarding the hyperparameters can be found in Appendix E.1.

Table 5: Hyperparameters and architectural decisions for our GdVAE model configurations on MNIST, CIFAR-10, and CelebA. Values specific to binary classification scenarios (MNIST - binary 0/1, CelebA) that include the use of consistency loss are enclosed in parentheses, if they differ from the parameters used in other experiments. The ADAM optimizer is consistently employed across all datasets.

	MNIST	CIFAR-10	CelebA
Batch size	64	64	64
Learning rate	0.0005	0.0005	0.0005
Epochs	24	24	24
Number classes K	10(2)	10	2
Latent dimension M	10	64	64
Latent dimension L	10(4)	10	4
Samples S in Algorithm 1	20	20	20
Samples for $\mathbb{E}$ in Eq. (11)	(10)	-	(10)
ϵ for $p(\delta) = \mathcal{U}(-\epsilon, \epsilon)$	(2.94)	-	(2.94)
Samples O for $\mathbb{E}$ in Eqs. (7) and (8)	1	1	1
Iterations T in Algorithm 1	3	3	3

Table 6: Prior encoder and label embeddings. In binary classification tasks, we opt for a class-independent choice of $\Sigma_z(y;\theta) = \Sigma_z(\theta)$. Consequently, we employ a distinct encoder network for the covariance $\Sigma_z(\theta)$, which is obtained by utilizing a constant input, $y = 1$.

Prior Encoder $p_\theta(z\|y) = \mathcal{N}\left(\mu_z(y;\theta), \Sigma_z(y;\theta)\right)$
Input: K values FC: L values $\Rightarrow$ FC: L values $\Rightarrow$ FC: L values FC ($\times 2$): $\dim(z) = M$ values
Encoder Label Embedding for y in $q_\phi(z\|x, y)$
Input: K values $\Rightarrow$ FC: 1 channel, $W \times H$ image
Decoder Label Embedding for y in $p_\theta(x\|y, z)$
Input: K values $\Rightarrow$ FC: 1 value

Table 7: Architecture for CelebA. We center crop and resize the images to have a width and height of $(W \times H) = (64 \times 64)$ and keep the three channels $C = 3$. The class label y is incorporated into the input image as a fourth channel through a label embedding (Tab. 6). The latent space's dimensionality is defined as $\dim(z) = M = 64$. We utilize $q_\phi(z|x,y) = \mathcal{N}\left(\mu_z(x,y;\phi), \Sigma_z(x,y;\phi)\right)$, with diagonal covariance matrix $\Sigma_z(x,y;\phi) = \text{diag}\left(\sigma^2_{z_1|x,y}, \ldots, \sigma^2_{z_M|x,y}\right)$.

Encoder $q_\phi(z\|x,y)$	**Decoder** $p_\theta(x\|y,z)$
Input: $4 \times 64 \times 64$	Input: $\dim(z) + 1 = M + 1$ values
Conv2d: 32 channels, 4×4 kernel, s=2, p=1	FC: 256 channels, 1×1 image
Conv2d: 32 channels, 4×4 kernel, s=2, p=1	ConvT2d: 64 channels, 4×4 kernel
Conv2d: 64 channels, 4×4 kernel, s=2, p=1	ConvT2d: 64 channels, 4×4 kernel, s=2, p=1
Conv2d: 64 channels, 4×4 kernel, s=2, p=1	ConvT2d: 32 channels, 4×4 kernel, s=2, p=1
Conv2d: 256 channels, 4×4 kernel	ConvT2d: 32 channels, 4×4 kernel, s=2, p=1
FC: $2 \cdot \dim(z) = 2 \cdot M$ values	ConvT2d: 3 channels, 4×4 kernel, s=2, p=1
Output: M values for $\mu_z(x,y;\phi)$ and $\log \Sigma_z(x,y;\phi)$	Output: $3 \times 64 \times 64$ image for $\mu_x(y,z;\theta)$

Table 8: Architecture for CIFAR-10.

Encoder $q_\phi(z\|x,y)$	**Decoder** $p_\theta(x\|y,z)$
Input: $4 \times 32 \times 32$	Input: $\dim(z) + 1 = M + 1$ values
Conv2d: 64 channels, 4×4 kernel, s=2, p=1	FC: 256 channels, 1×1 image
Conv2d: 128 channels, 4×4 kernel, s=2, p=1	ConvT2d: 256 channels, 2×2 kernel
Conv2d: 256 channels, 4×4 kernel, s=2, p=1	ConvT2d: 256 channels, 2×2 kernel, s=2
Conv2d: 256 channels, 2×2 kernel, s=2	ConvT2d: 128 channels, 4×4 kernel, s=2, p=1
Conv2d: 256 channels, 2×2 kernel	ConvT2d: 64 channels, 4×4 kernel, s=2, p=1
FC ($\times 2$): $\dim(z) = M$ values	ConvT2d: 3 channels, 4×4 kernel, s=2, p=1
Output: M values for $\mu_z(x,y;\phi)$ and $\log \Sigma_z(x,y;\phi)$	Output: $3 \times 32 \times 32$ image for $\mu_x(y,z;\theta)$

Table 9: Architecture for MNIST.

Encoder $q_\phi(z\|x,y)$	**Decoder** $p_\theta(x\|y,z)$
Input: $2 \times 28 \times 28$	Input: $\dim(z) + 1 = M + 1$ values
Conv2d: 64 channels, 6×6 kernel, s=2	FC: 256 channels, 4×4 image
Conv2d: 128 channels, 5×5 kernel	ConvT2d: 128 channels, 5×5 kernel
Conv2d: 256 channels, 5×5 kernel	ConvT2d: 64 channels, 5×5 kernel
FC ($\times 2$): $\dim(z) = M$ values	ConvT2d: 1 channel, 6×6 kernel, s=2
Output: M values for $\mu_z(x,y;\phi)$ and $\log \Sigma_z(x,y;\phi)$	Output: $1 \times 28 \times 28$ image for $\mu_x(y,z;\theta)$

Table 10: Architecture for FFHQ.

Encoder $q_\phi(z\|x,y)$	**Decoder** $p_\theta(x\|y,z)$
Input: $2 \times 96 \times 96$	Input: $\dim(z) + 1 = M + 1$ values
Conv2d: 32 channels, 4×4 kernel, s=2, p=1	FC: 256 channels, 1×1 image
Conv2d: 32 channels, 4×4 kernel, s=2, p=1	ConvT2d: 128 channels, 3×3 kernel, s=1, p=0
Conv2d: 64 channels, 4×4 kernel, s=2, p=1	ConvT2d: 64 channels, 4×4 kernel, s=2, p=1
Conv2d: 64 channels, 4×4 kernel, s=2, p=1	ConvT2d: 64 channels, 4×4 kernel, s=2, p=1
Conv2d: 128 channels, 4×4 kernel, s=2, p=1	ConvT2d: 32 channels, 4×4 kernel, s=2, p=1
Conv2d: 256 channels, 3×3 kernel, s=1, p=0	ConvT2d: 32 channels, 4×4 kernel, s=2, p=1
FC: $2 \cdot \dim(z) = 2 \cdot M$ values	ConvT2d: 1 channel, 4×4 kernel, s=2, p=1
Output: M values for $\mu_z(x,y;\phi)$ and $\log \Sigma_z(x,y;\phi)$	Output: $1 \times 96 \times 96$ feature map for $\mu_x(y,z;\theta)$

C.3 Details of Baseline Models and Assets

Black-Box Baseline. The optimal baseline for evaluating the predictive performance of the GdVAE in Tab. 2 involves training a discriminative classifier and a CVAE jointly. Unlike the GdVAE architecture, this classifier employs a separate neural network as its backbone. This backbone network replicates the structure of the CVAE's encoder (refer to Tabs. 7 to 9), allowing the CVAE to learn an optimal representation for reconstruction, while the discriminative classifier learns an independent representation for classification.

The classifier leverages the CVAE encoder without the additional class input to generate a latent representation z. Subsequently, this latent vector is processed by a one-layer fully connected neural network, which uses a softmax function to map z to the class output.

Importance Sampling (IS) [45, 48, 54] for Generative Classification. An alternative approach to our EM-based inference is presented in [48], where they use separate VAEs for different classes and perform an importance sampling strategy to obtain a generative classifier. We extend this approach to CVAEs and use the importance sampling strategy as a baseline in Tab. 2. The importance sampling strategy for CVAEs to approximate the likelihood $p_\theta(x|y)$ is given by

$$p_\theta(x|y) = \mathbb{E}_{z\sim p_\theta(z|y)}[p_\theta(x|y,z)] = \int p_\theta(x|y,z)p_\theta(z|y)dz \tag{24}$$

$$\approx \frac{1}{S}\sum_{s=1}^{S} \frac{p_\theta(x|y,z^{(s)})p_\theta(z^{(s)}|y)}{q_\phi(z^{(s)}|x,y)}, \tag{25}$$

where the samples $z^{(s)}$ are drawn from $q_\phi(z|x,y)$ and the likelihood is afterwards used in a Bayes' classifier $p_\theta(y|x) = \eta p_\theta(x|y)p_\theta(y)$. The drawback of this approach is that in addition to the encoder it requires to invoke the decoder model for each sample and since the dimensionality of the input space $x \in \mathbb{R}^N$ is typically larger than the dimensionality of the latent space $z \in \mathbb{R}^M$, more samples are required for a good approximation.

This baseline method is denoted by importance sampling (IS) in Tab. 2. The architecture and learning objective remain unchanged, but instead of using Algorithm 1, importance sampling in the image space is employed. For a fair comparison, we utilize $S = 60$ for the importance sampling method. This is in line with the GdVAE, which uses $S = 20$ samples but conducts $T = 3$ iterations, resulting in a total of 60 samples as well.

ProtoVAE [13] (https://github.com/SrishtiGautam/ProtoVAE). We utilized the original implementation as detailed in [13]. In our adaptation, we substituted the backbone network with the GdVAE backbone and configured the model to work with a single prototype. Furthermore, we explored various hyperparameter settings, such as adjusting the loss balance to match our reconstruction loss and binary cross-entropy loss. The results are presented in Tab. 13.

GANalyze [15] (http://ganalyze.csail.mit.edu/). We utilized the original implementation as detailed in [15]. The code already includes a PyTorch version,

which is mainly used for the implementation of the so called transformer $T(z, \alpha)$. The transformer is equivalent to a linear explainer function

$$\mathcal{I}_f(z, \alpha, k) = z^\alpha = z + \alpha w^{(k)}, \tag{26}$$

where α is the requested confidence for the counterfactual class and $w^{(k)}$ is the direction that is learned for each counterfactual class k. As in the original implementation we use a quadratic loss between the desired confidence and the classifier output and utilize the per sample loss

$$\mathcal{L}_{cf}(x^\alpha, \alpha, k) = \left[p_\theta(y = k|x^\alpha) - \alpha\right]^2, \tag{27}$$

where k is the counterfactual class with respect to the class label c of the input image x, $x^\alpha = \mathcal{I}_f(h(x), \alpha, k)$ the counterfactual, and h the encoder. We optimize GANalyze by approximating the expectation in

$$\mathcal{L}^{GANalyze}(w) = \mathbb{E}_{\alpha \sim \mathcal{U}(0,1)}[\mathcal{L}_{cf}(x^\alpha, \alpha, k)] \tag{28}$$

with 10 samples for each training image. GANalyze's primary objective is to learn a vector $w^{(k)}$ for each class, as opposed to a single vector as seen in GdVAE. Instead of using a GAN, we leverage our pre-trained GdVAE as an encoder, decoder, and classifier. The conditional decoder takes the counterfactual class k as its input. Moreover, we have explored various hyperparameter settings. For instance, one such setting involves the use of normalization, a practice not documented in the paper but applied in the code.

This normalization enforces the counterfactual distance from the origin to be identical to the original input $z = h(x)$

$$\mathcal{I}_f^{norm}(z, \alpha, k) = \frac{\mathcal{I}_f(z, \alpha, k)}{\|z\|_2}. \tag{29}$$

The results of various hyperparameter settings are presented in Tab. 12.

UDID [49] (https://github.com/anvoynov/GANLatentDiscovery). We utilized the original implementation as detailed in [49]. The code already includes a PyTorch version, which is mainly used for the implementation of the so called latent deformator $A(\alpha e_k)$ and reconstructor $R(x, x^\alpha)$ that are employed for unsupervised latent space analysis. The deformater is a non-linear explainer function

$$\mathcal{I}_f(z, \alpha, k) = z^\alpha = z + A(\alpha e_k), \tag{30}$$

where $e_k \in \mathbb{R}^K$ are standard unit vectors defining the directions, one for each class. $\alpha \sim \mathcal{U}(0, 1)$ defines the strength of manipulation and $A(\cdot) \in^{M \times K}$ is defined by a neural network. The primary objective of the reconstructor $R(x, x^\alpha) = (\hat{k}, \hat{\alpha})$ is to compare the original image x and the manipulated version x^α, aiming to replicate the manipulation in the latent space. Consequently, the method seeks to discover disentangled directions. Instead of employing a GAN, we utilize our pre-trained GdVAE as an encoder, decoder, and classifier. Additionally, we

introduce a supervised learning component $\mathcal{L}_{cf}$ to align the method with other supervised CF methods. We therefore employ a per-sample loss defined by

$$\mathcal{L}^{UD}(A) = \mathbb{E}_{\alpha}\Big[\mathcal{L}_{cl}(k, \hat{k}) + \lambda \mathcal{L}_r(\alpha, \hat{\alpha}) + \mathcal{L}_{cf}(x^{\alpha}, \alpha, k)\Big], \tag{31}$$

where $\lambda = 0.25$ represents the weight for the regression task, $\mathcal{L}_{cl}$ corresponds to the cross-entropy function, $\mathcal{L}_r$ pertains to the mean absolute error, and $\mathcal{L}_{cf}$ denotes the supervised loss for the counterfactuals. The supervised loss aligns with the one used in GANalyze (as in Eq. (27)). We use a sample size of 10 for α to approximate the expectation. The results of various hyperparameter settings are presented in Tab. 12. To enhance the method and refine the proximity property, we incorporated a proximity loss $\mathcal{L}_{prox}(x, x^{\alpha}) = \|x - x^{\alpha}\|_2^2$, aiming to maintain close resemblance between the counterfactual and query images.

ECINN [21]. ECINN employs an invertible neural network and applies a post-hoc analysis of class conditional means within the latent space to determine an interpretable direction. They make the assumption that the covariance matrix Σ_z (see Sec. 3.1) is the identity matrix. Their post-hoc method is similar to our local-L2 function, but it approximates the true classifier using empirical mean values. Consequently, we view ECINN as an empirical implementation of our method, additionally estimating the empirical covariance.

Furthermore, they create two counterfactuals: one with high confidence for the opposing class and another precisely at the decision boundary. We replicate and extend their approach by using our explainer function (refer to Eq. (10)), wherein we empirically determine class conditional mean values and the covariance matrix after training the GdVAE. Thus, we employ $\overline{w} = \overline{\Sigma}_z^{-1}(\overline{\mu}_{z|k} - \overline{\mu}_{z|c})$, utilizing the empirical means $\overline{\mu}_{z|\cdot}$ and covariance $\overline{\Sigma}_z$ with the predicted class of the GdVAE as label. The formula for the counterfactual at the decision boundary is exactly the one that ECINN would employ.

AttFind [30] (https://github.com/google/explaining-in-style). We utilized the original implementation as detailed in [30]. To accommodate our PyTorch-based model, we translated their TensorFlow implementation of the *AttFind* method. It's important to emphasize that our usage of the AttFind method is solely for identifying significant directions within the latent space of our GdVAE. We do not employ their GAN architecture.

The AttFind method operates by iterating through latent variables, evaluating the impact of each variable on the classifier's output for a given image, and subsequently selecting the top-k significant variables. An image is considered explained once AttFind identifies a manipulation of the latent space that leads to a substantial alteration in the classifier's output, effectively changing the classifier's class prediction. We employ their *Subset* search strategy, which focuses on identifying the top-k variables where jointly modifying them results in the most significant change in the classifier's output. This method is limited to producing class flips and is not intended for generating CFs with desired confidence values. Hence, we have labeled this method with AttFind† to denote its original purpose of effecting class changes only. The results are presented in Tab. 15, though their accuracy and MSE may not be directly comparable to those in Tab. 3.

EBPE [43] (https://github.com/...by_Progressive_Exaggeration). We utilized the original implementation as detailed in [43]. To accommodate our PyTorch-based model, we translated their TensorFlow implementation. The most significant modification involves replacing the GAN with the CVAE architecture utilized by all approaches. EPBE, aside from GdVAE, uniquely required decoder training, resulting in distinct latent space characteristics and reconstruction quality. EBPE solely uses the pre-trained GdVAE for classification.

The original EBPE version was designed to work with the CelebA dataset, which is more complex than the MNIST dataset. The MNIST classifier we aimed to explain achieved remarkably high accuracy and confidence, resulting in some bins within the EBPE training having no samples for generating images at specific confidence values. When a bin lacked any samples, it was impossible to generate additional images from it. This issue could be addressed through hyperparameter tuning. For hyperparameter analysis, we define the loss

$$\begin{aligned}\mathcal{L}^{EBPE} &= \lambda_{cGAN}\mathcal{L}_{cGAN}(G,D) + \lambda_{rec}\mathcal{L}_{rec}(G) \\ &\quad + \lambda_{cyc}\mathcal{L}_{cyc}(G) + \lambda_{cfCls}\mathcal{L}_{cfCls}(G) + \lambda_{recCls}\mathcal{L}_{recCls}(G). \end{aligned} \tag{32}$$

Here, $\mathcal{L}_{cGAN}$ represents EBPE's conditional GAN loss, $\mathcal{L}_{rec}$ is the reconstruction loss, $\mathcal{L}_{cyc}$ denotes the cycle loss, $\mathcal{L}_{cfCls}$ is the classification loss for the counterfactual, and $\mathcal{L}_{recCls}$ stands for the classification loss for the reconstruction of the input image. λ represents the weight of the corresponding loss. For further details, please see [43] and the original implementation. Detailed results for different configurations can be found in Tab. 12.

As highlighted in the 'Limitations' section, the results showcased in the main paper utilized 24 epochs to maintain uniformity across all methods. For improved EBPE performance with extended training, see the 96-epoch results in Tab. 12.
C3LT [26] (https://github.com/khorrams/c3lt). We utilized the original implementation as detailed in [26]. C3LT was initially designed for use with pre-trained models, and we applied this implementation to our GdVAE models.

While C3LT was originally tailored for the simpler consistency task of class modification without explicitly requesting a user-defined confidence, we extended its functionality by introducing a supervised loss term, denoted as $\mathcal{L}_{cf}$. This loss term serves to align the user-requested confidence level (α) with the predicted confidence ($\hat{\alpha}$), with $\hat{\alpha} = p_\theta(y = k|\mathcal{I}_f(h(x), \alpha, k))$. For $\mathcal{L}_{cf}$, we experimented with both quadratic (Eq. (27)) and cross-entropy functions to assess their performance. The results of these experiments can be found in Tab. 12.

In conclusion, we leveraged C3LT to facilitate these modifications and added a supervised loss term to ensure alignment between the requested confidence and the model's predictions. The original version, without the added loss term, is referred to as C3LT† in Tab. 15.

C.4 Compute Resources

For training our GdVAE and baseline models, we had the option to utilize two high-performance PCs equipped with multiple GPUs. The first PC featured an Nvidia RTX 3090 and a Titan RTX, both boasting 24 GB of memory each. The second PC made use of two Nvidia A6000 GPUs, each equipped with 48 GB of memory. To establish a reference point for the required computational time, we considered the GdVAE exclusively for the counterfactual tasks, as they represent an upper limit for the models' demands.

For an individual epoch on binary MNIST, it took 5 minutes, and for CelebA, it took 60 minutes on the A6000. In the context of our hyperparameter sweep, we explored 25=(5+8+6+6) different model configurations for MNIST and 12 for CelebA, encompassing parameters like the number of samples S, iterations T, the balance between α/β, and the consistency weight γ. Each of these configurations underwent four separate training runs to calculate the mean and standard deviations, ultimately leading to the training of 100 models for MNIST and 48 for CelebA, respectively.

Consequently, the total computational time required for this parameter analysis sums up to $(5\ ^{min}/_{epochs} \cdot 100 \cdot 24\ epochs + 60\ ^{min}/_{epochs} \cdot 48 \cdot 24\ epochs) = 81120\ min$, which is equivalent to 1352 h of GPU time.

D Evaluation Metrics

D.1 Metrics for Predictive Performance in Tab. 2

Accuracy (ACC). In Tab. 2, we assess the predictive performance of the classifier using the accuracy (ACC) metric, defined as

$$ACC = \frac{1}{D} \sum_{d=1}^{D} \mathbb{1} \left\{ \hat{y}^{(d)} = y^{(d)} \right\}, \tag{33}$$

with the indicator function $\mathbb{1}\{\cdot\}$. Here, $\hat{y}$ is the class prediction, determined as the class with the highest probability according to $\hat{y} = \arg\max_i p_\theta(y = i|z)$. The ground-truth class labels are denoted by $y \in \{1, \ldots, K\}$ and we have D test data samples. $y^{(d)}$ represents the d-th sample.

Mean Squared Error (MSE). To evaluate the reconstruction quality in Tab. 2, we calculate the mean squared error (MSE) between the ground-truth input image x and the reconstructed image $\hat{x}$

$$MSE = \frac{1}{D \cdot N} \sum_{d=1}^{D} \sum_{i=1}^{N} \left(x_i^{(d)} - \hat{x}_i^{(d)} \right)^2. \tag{34}$$

We assume images to be vectorized, with $x \in \mathbb{R}^N$. Here, N is defined as the product of the image's width (W), height (H), and number of channels (C), i.e., $N = W \cdot H \cdot C$. $x^{(d)}$ represents the d-th sample.

D.2 Metrics for CF Explanations in Tab. 3

Realism. Realism in counterfactuals is essential, as they should resemble natural data. To assess realism, we employ the *Fréchet Inception Distance (FID)* metric, a standard measure for this purpose [14, 26, 43]. We compute the FID values using the PyTorch implementation from [41].

Consistency. CF explanations aim to influence the behavior of a classifier to obtain desired outcomes. In case of our method the consistency task is to guarantee that the requested confidence value p_c accurately matches to the confidence prediction of the classifier $\widehat{p}_c = p_\theta(y = c|h(g(z^\delta)))$ for the CF $z^\delta = \mathcal{I}_f(z, \delta)$. c is consistently assigned to the class label of the original input.

As demonstrated in [43], a method for assessing consistency is to create a plot that compares the expected classifier outcomes with the confidence predictions of the classifier for the generated CF. The optimum is reached when we obtain an identity relationship ($p_c = \widehat{p}_c$) between the two quantities. We use kernel density estimates (KDE) to visualize this relationship (Figs. 10 and 17).

Similar to [14], we quantitatively evaluate the existence of a linear relationship using the *Pearson correlation coefficient*. In addition, we utilize the *mean squared error (MSE)* between the desired p_c and the estimated confidence $\widehat{p}_c$

$$MSE = \frac{1}{D^\star} \sum_{d=1}^{D^\star} \left(p_c^{(d)} - \widehat{p}_c^{(d)} \right)^2 . \tag{35}$$

Here, we have $D^\star$ samples and $p_c^{(d)}$ represents the d-th sample. Given that we request confidence values within the range $p_c \in [0.05, 0.95]$, with a step size of 0.05, we acquire 19 counterfactuals per test image. As a result, $D^\star = 19 \cdot D$, where D represents the number of test images.

Accuracy (ACC). Finally, the accuracy metric, as defined in [26] and denoted by "Val", is designed for the simpler consistency task, which assesses only class flips as a binary classification problem. To evaluate continuous confidence requests, we employ 12 bins $b \in \{1, \ldots, 12\}$ and treat the bin assignment of the prediction as a multi-class problem. Therefore, we use Eq. (33) with ground-truth bins $b^{(d)}$ and predicted bins $\hat{b}^{(d)}$ for the $D^\star$ samples.

In particular, ACC and MSE are used to gauge whether the counterfactuals are predominantly generated at the extreme confidence levels, near one or zero. While the results may not be directly comparable, in the context of methods that focus solely on generating class flips, such as C3LT† [26] and AttFind† [30], we adopt accuracy with two bins as a reference point, as per the definition in [26] for binary classification. Please note that this task is considerably simpler, resulting in accuracy values in Tab. 15 being close to 100% for methods marked with †.

Proximity. The CF should only change the input in a minimal way $x^\delta = \arg\min_{x'} \rho(x, x')$, with respect to some user defined quantity $\rho(\cdot)$, *e.g.*, $\rho(x, x') = \|x - x'\|_2$ [4].

Mean Squared Error (MSE). In [26] they measure proximity by means of the $L1$-norm between the query image x and the counterfactuals x^δ. We adopt this metric by using Eq. (34) for the $D^\star$ counterfactual samples.

E Additional Results

E.1 GdVAE Hyperparameter Analysis

Parameterization of the Loss Function. Before arriving at the final loss, we conducted several initial experiments on the MNIST dataset. Initially, we compared our loss formulation (A) derived from Eq. (12) with the loss formulation (B1) outlined in Sec. 3.1, where the training process is streamlined with the inference process. Additionally, we fine-tuned the reconstruction and classification loss by adjusting the scale of the reconstruction loss using $p_\theta(x|y,z) = \mathcal{N}(\mu_x(y,z;\theta), \Sigma_x(y,z;\theta))$, with $\Sigma_x := \Sigma_x(y,z;\theta) = 0.6^2 \cdot I$ for likelihood calculation (as in [12]), instead of the standard $\Sigma_x = I$. Furthermore, the cross-entropy loss for classification was rescaled in proportion to the image size, using the factor $0.1 \cdot W \cdot H \cdot C$ (B2), where W, H, and C represent the width, height, and channels of the input image, respectively. Finally, using two priors $p(z|y)$ and $p(z)$ is not essential, but they are part of the model. In our probabilistic view, the used factorization (see Sec. 3) justifies including $p(y|z)$ (and thereby $p(z)$), in contrast to works that merely append $p(y|.)$. However, using an uniform prior for $p(z)$, akin to excluding $p(z)$ from the loss, is valid. For MNIST, incorporating the normal prior results in a lower reconstruction error.

The results pertaining to these settings, including classification accuracy (ACC) and mean squared error (MSE) as a metric for reconstruction quality, are presented in Tab. 11. We adopted the B2 setting for all other experiments and datasets without dataset-specific fine-tuning.

Table 11: Evaluation of different loss functions and settings of the GdVAE on the MNIST dataset. We use $\alpha = \beta = 1$, $S = 20$, and $T = 3$. MSE is scaled by a factor of 10^2. Mean values, including standard deviation, are reported over four training processes with different seed values.

Setting	Details	$ACC\% \uparrow$	$MSE \downarrow$
A:	Eq. (12), $\Sigma_x = I$	88.6±1.25	1.19±0.04
B1:	Eqs. (7) and (8), $\Sigma_x = I$	96.0±0.85	1.04±0.02
B2:	Eqs. (7) and (8), $\Sigma_x = 0.6^2 \cdot I$	99.0±0.11	1.10±0.04
B2 w/o $p(z)$**:**	Eqs. (7) and (8), $\Sigma_x = 0.6^2 \cdot I$	99.0±0.08	1.14±0.03

How to Parameterize the EM-Based Algorithm? The GdVAE (Algorithm 1) requires user-defined values for the number of iterations (T) and samples (S). To determine the optimal number of iterations, we assess the stability of the training process on the MNIST dataset. The evaluation involves measuring the entropy of $q_\phi(y|x)$ during training epochs and comparing successive epochs. The results, depicted in Fig. 6, illustrate the change in entropy with increasing iterations, averaged over the entire test dataset. The error bars represent the standard error across four training runs with different seeds. Convergence is observed after 3 iterations. Other parameters are set to $\alpha = \beta = S = 1$. Based on the convergence analysis, we fix the value of T to 3 for subsequent experiments.

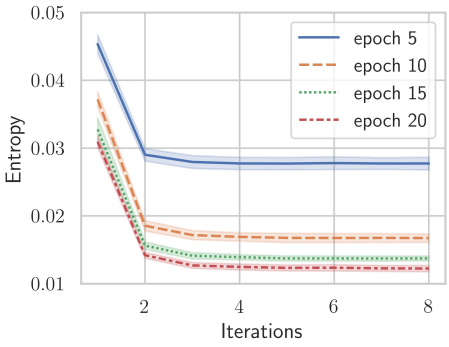

Fig. 6: Evaluation of number of iterations T during the training process on the MNIST dataset. Mean values, including standard error, are reported over four training processes with different seed values.

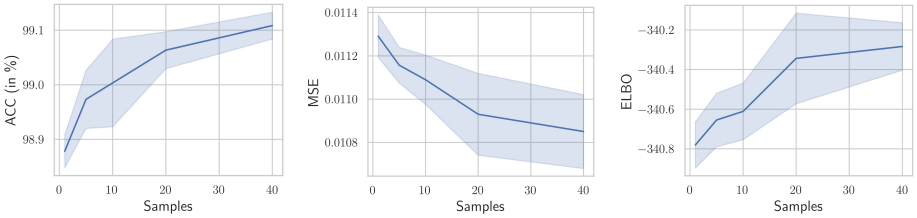

Fig. 7: Quality of models trained on the MNIST dataset with a different number of samples S.

After assessing convergence, we examine the influence of the number of samples S drawn from $q_\phi(z|x)$ on performance. We evaluate classification accuracy (ACC), reconstruction error (MSE), and the average ELBO of M1 and M2 through multiple training sessions with different random seeds using $S \in \{1, 5, 10, 20, 40\}$ and report the average values along with the standard error. The results, depicted in Fig. 7, demonstrate the expected improvement in performance with an increasing number of samples. All model trainings are stable and result in accuracy values $\geq 98\%$ and for $S \in \{20, 40\}$ comparable results are obtained with a small standard error regarding classification accuracy. By selecting $S = 20$, a balanced trade-off between computational load and performance is achieved, as indicated by the evidence lower bound (ELBO).

How to Balance the Loss for Models M1 and M2? The proposed GdVAE model incorporates two types of loss functions: the M1 and M2 losses. Both losses include the reconstruction loss, but differ primarily in their impact on the recognition model $q_\phi(z|x, y)$ and the classifier. While M1 focuses on training the likelihood model for purely generative classification, M2 provides a discriminative training signal for the generative classifier and enforces a standard normal distribution in the latent space. As described in Sec. 3.1, we ensure alignment

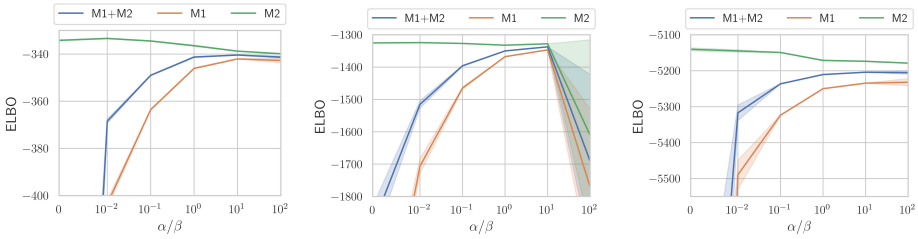

(a) MNIST **(b)** CIFAR-10 **(c)** CelebA

Fig. 8: Analysis of the optimal balance between models M1 and M2 on MNIST, CIFAR-10, and CelebA datasets. Mean values, including standard error, are reported over four training processes with different seed values.

between the training and inference processes, requiring both models to utilize the EM-based classifier for calculating the reconstruction loss using $p_\theta(x|z,y)$. For the EM algorithm to function properly, a prerequisite is that, given an input image x, the recognition model $q_\phi(z|x,y)$ must either have the lowest Kullback-Leibler divergence $KL(q_\phi(z|x,y)||p_\theta(z|y))$ for the correct class or be independent of y (*e.g.*, [12]). The M1 loss does not consider these aspects, as it solely focuses on minimizing $KL(q_\phi(z|x,y)||p_\theta(z|y))$ for the correct class without enforcing it to be smaller than for the other classes. The desired behavior is enforced by adding the M2 loss, which incorporates a discriminative training signal and a KL divergence term that promotes independence. Furthermore, the classifier utilized in M2 relies on the likelihood function learned in M1, highlighting the interdependence between both models.

We analyze the optimal interplay between models M1 and M2 by evaluating the parameterization of the loss function defined by Eqs. (7) and (8), where we select suitable values for α and β. To keep notation concise, we use the ratio α/β instead of the individual values. We assess combinations of α and β from the set $\{0, 1, 10, 100\}$ and present the ELBO results graphically in Fig. 8. The results indicate that assigning equal weight values to the models ($\alpha/\beta = 1$) or using $\alpha/\beta = 10$ generally yields good performance across diverse datasets. To slightly enhance classification accuracy, we opted for $\alpha/\beta = 1$ in all experiments discussed in the main paper. For the MNIST dataset, opting for $\alpha/\beta = 1$ led to an accuracy of 99.0%, as opposed to 98.8% with nearly identical reconstruction error. Similar accuracy improvements were observed for CIFAR-10 (65.1% and 63.4%) and CelebA (96.7% and 96.4%) datasets. These results are used in Tab. 2.

How to Balance the Consistency Loss? The experiments aim to assess the quality of counterfactuals (CF) when varying the impact of the consistency loss. As in the main paper, we employ the Fréchet Inception Distance (FID) to gauge *realism* and Pearson and Spearman's rank correlation coefficients to gauge *consistency*. Following a similar approach to [43], we also visualize the requested versus the actual response of the classifier using a kernel density estimate plot.

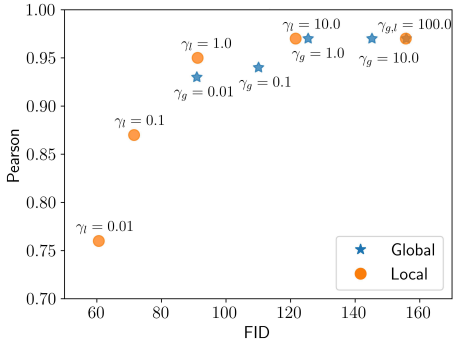

Fig. 9: Pearson correlation against FID scores on the MNIST dataset, where γ_l represents the consistency weight for the local method, and γ_g for the global one.

The ablation study, examining the influence of the consistency loss, is depicted in Fig. 10. We assess weight values λ for the consistency loss from the set $\{0.0, 0.01, 0.1, 1.0, 10, 100\}$. The error bars represent the standard error across four training runs with different seeds. We present results for both our local-L2 and global CF generation methods, as described in the main paper Sec. 3.2. $x^\star$ serves as the FID baseline, representing values obtained by applying the encoder and decoder directly to the test data. Thus, the FID score for $x^\star$ reflects the reconstructed test set.

The ablation study on the consistency loss in Fig. 10 reveals a trade-off between *consistency* and *realism*. When the consistency parameter exceeds $\lambda = 1$, the FID score of the ground truth reconstructions is significantly affected. Similarly, as the influence of the consistency regularizer increases, the correlation and FID value also increases. In Fig. 9, we visualize this trade-off by directly plotting the Pearson correlation against the FID scores.

The KDE plot uncovers an intriguing observation: even without utilizing the consistency regularizer, reasonable counterfactual examples can be generated with high correlation values ($\rho_p \approx 0.9$). Interestingly, counterfactuals tend to be generated at the extreme ends of the confidence range, near one or zero. Therefore, the method effectively flips the class of the query image, but the confidence values are not well calibrated. With increasing correlation values and improved calibration, the realism measure (FID) yields inferior results. One possible explanation is that more counterfactuals are generated near the decision boundary, where there is less real data available, resulting in a compromised natural appearance. It becomes evident that, for the consistency task [26, 30, 40] in which the user solely pre-defines the class label without specifying the confidence level, generating realistic images with low FID scores is considerably easier. Furthermore, we observe that global CF generation exhibits greater consistency with the classifier but lags behind in terms of realism when compared to the local CF generation process. The KDE plots for each model's four training runs are displayed in Fig. 17. These are the models used in Tab. 3.

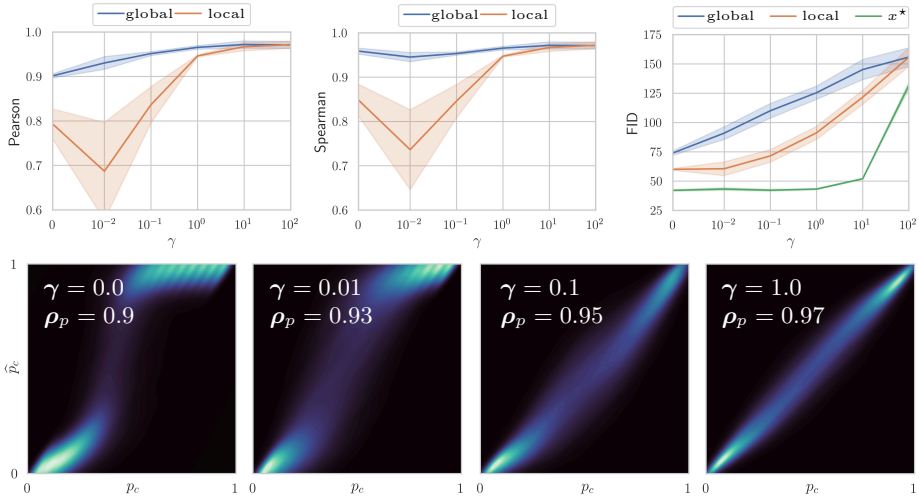

Fig. 10: Consistency of counterfactual examples using the MNIST dataset. Top: Pearson's ρ_p and Spearman correlation coefficients assess the relationship between the requested confidence and the classifier's output for counterfactual examples. Significance in correlation is indicated by a $p-value \leq 0.001$. Similarly, the Fréchet Inception Distance (FID) quantifies the image quality of the generated counterfactuals in comparison to the real data. Mean values, including standard error, are reported over four training processes with different seed values. Bottom: Consistency of the requested confidence versus the actual classifier confidence is visually depicted using a kernel density estimate (KDE) plot of the observations. The desired confidence output of the classifier for a counterfactual example x^δ is specified by p_c, while the actual confidence acquired by inputting the counterfactual to our classifier is represented by $\widehat{p}_c = p(y = c|x^\delta)$. Additionally, the corresponding Pearson correlation coefficient ρ_p is visualized.

E.2 Analysis of Baseline Models

We conducted explorative parameter tuning for all baseline models, initially using the parameterization from the original implementation. Subsequently, we fine-tuned the parameters based on the results to achieve a balanced performance across various metrics and datasets. Results regarding ProtoVAE can be found in Tab. 13 and the results for the counterfactual methods are presented in Tabs. 12 and 15. Additionally, Tab. 14 presents the GdVAE realism results for various ranges of query confidences for comparison with Tab. 12. In the main paper, the FID scores for $p_c \in [0, 1]$ are reported.

ProtoVAE [13]. The hyperparameter analysis for ProtoVAE is detailed in Tab. 13. Setting A represents the original parameterization of the loss function as introduced by [13]. In an effort to enhance results, we modified the loss function based on our GdVAE settings, outlined in Tab. 11. Initially, we adjusted the scale of the reconstruction loss using $p_\theta(x|y,z) = \mathcal{N}(\mu_x(y,z;\theta), \Sigma_x(y,z;\theta))$, with $\Sigma_x := \Sigma_x(y,z;\theta) = 0.6^2 \cdot I$ for likelihood calculation (B1), maintaining the original weighting of the other loss terms. Setting B2 involves adjusting

Table 12: CF explanations across diverse baseline model configurations. Mean values, with standard deviation, are reported across four training runs with different seeds. The configurations used in the main paper's experiments (Tab. 3) are **bolded**.

	Setup	Consistency			Realism (FID) ↓		
		$\rho_p \uparrow$	$ACC\% \uparrow$	$MSE \downarrow$	$\widehat{p}_c \notin [0.1, 0.9]$	$\widehat{p}_c \in [0.1, 0.9]$	$\widehat{p}_c \in [0, 1]$
				GANalyze [15]			
MNIST Binary 0/1	A	0.48±0.04	2.8±0.8	19.33±1.31	79.88±10.04	110.36±8.54	55.77±7.46
	B1	0.84±0.04	5.5±1.3	6.75±1.27	51.65±5.25	96.20±8.93	54.89±4.19
	B2	0.93±0.03	25.9±16.8	2.09±1.35	122.16±17.74	158.01±27.19	132.36±23.35
				UDID [49]			
MNIST Binary 0/1	A	0.87±0.02	13.1±5.9	5.91±1.04	159.16±21.48	181.54±29.72	155.37±17.39
	B1	0.87±0.03	0.6±0.2	8.47±0.12	46.74±4.34	104.99±12.26	42.98±3.93
	B2	0.85±0.01	1.2±0.3	8.82±0.18	42.01±1.84	104.11±10.33	38.89±2.01
	B3	0.80±0.01	2.9±0.5	10.45±0.16	45.90±1.01	104.46±7.61	42.40±1.14
	C	0.79±0.05	4.7±1.5	8.82±0.18	74.71±21.85	106.04±22.54	72.64±24.42
CelebA Smiling	A	0.98±0.01	71.5±6.8	0.24±0.13	411.09±22.61	381.26±24.01	370.69±19.59
	B2	0.86±0.06	15.8±9.2	4.22±2.17	146.58±43.18	217.36±96.52	178.23±75.84
				EBPE [43]			
CelebA Smiling	A	0.91±0.01	26.3±1.3	1.64±0.19	347.88±190.56	463.90±35.91	425.76±15.80
	B1	0.86±0.02	20.0±4.6	3.21±0.92	217.41±0.76	252.24±12.78	241.99±8.13
	B2	0.00±0.01	0.0±0.0	32.18±2.14	372.58±19.57	n/a	372.58±19.57
	B3	0.99±0.01	80.8±3.3	0.09±0.05	387.15±11.34	403.74±9.36	391.91±16.79
	C	0.94±0.01	41.9±3.1	1.22±0.16	193.99±20.44	191.90±20.66	191.67±20.51
	D1	0.97	54.39	0.56	185.17	185.16	184.96
	D2	0.96	53.62	0.57	148.02	146.75	146.73
	D3	0.96	53.71	0.57	120.45	120.14	120.00
				C3LT [26]			
MNIST Binary 0/1	A	0.84±0.08	2.0±0.8	4.71±2.21	94.13±12.06	106.90±14.25	92.30±19.59
	B	0.89±0.03	3.6±0.8	6.32±1.39	63.49±8.73	96.11±17.22	57.09±10.78
CelebA Smiling	A	0.89±0.04	3.5±2.5	3.52±0.71	122.29±12.06	138.82±15.33	133.13±13.56
	B	0.90±0.01	11.8±5.5	3.94±0.66	96.65±4.97	113.70±19.52	101.46±11.56

Table 13: Hyperparameter analysis of ProtoVAE. We report classifier's accuracy (ACC) and mean squared error (MSE) of the reconstructions. MSE is scaled by a factor of 10^2. Mean values, including standard deviation, are reported over four training processes with different seeds. Configurations for experiments in Tab. 2 are **bolded**.

	Setting	$ACC\% \uparrow$	$MSE \downarrow$
MNIST	**A: ProtoVAE** [13]	99.1±0.17	1.51±0.23
	B1	98.0±0.12	1.00±0.01
	B2	94.8±0.37	1.01±0.01
	B3	94.8±0.31	0.99±0.01
CIFAR-10	**A: ProtoVAE** [13]	76.6±0.35	2.69±0.02
	B1	58.4±1.31	0.92±0.02
	B2	31.2±2.18	0.85±0.05
	B3	30.0±3.25	0.37±0.02
CelebA Gender	**A: ProtoVAE** [13]	96.6±0.24	1.32±0.10
	B1	96.0±0.22	0.76±0.02
	B2	88.9±0.80	0.75±0.05
	B3	85.8±0.50	0.74±0.03

Table 14: FID evaluation of GdVAE's CF explanations for different confidence ranges.

	Method	Realism (FID) ↓		
		$\widehat{p}_c \notin [0.1, 0.9]$	$\widehat{p}_c \in [0.1, 0.9]$	$\widehat{p}_c \in [0, 1]$
MNIST	**Ours** (global)	126.93±8.73	140.11±9.04	125.45±11.32
Binary 0/1	**Ours** (local-L2)	91.80±10.35	101.25±11.07	91.22±11.04
CelebA	**Ours** (global)	118.40±5.15	138.79±6.11	128.93±4.94
Smiling	**Ours** (local-L2)	86.01±2.60	86.59±2.47	85.52±2.37

the weight of the reconstruction and classification loss according to our GdVAE learning objective. Finally, setting B3, an extension of B2, incorporates a change in the learning rate from 0.001 to the one used by our GdVAE, which is 0.0005. As intended, we achieved a consistent reduction in reconstruction error; however, this improvement came at the cost of lower classification accuracy. Hence, we retained the parameterization from the original implementation.

GANalyze [15]. All hyperparameter tuning for GANalyze was done on the MNIST binary dataset and the results can be found in Tab. 12. In the initial setting (A), we employed the loss function from the original implementation, which included the normalization of counterfactuals. In the second setting (B1), we recreated the loss as described in the paper, omitting the normalization and achieving enhanced results. To further explore the efficacy of setting B1, we extended the training to 48 epochs (setting B2) instead of the original 24 epochs.

UDID [49]. The hyperparameter tuning for UDID primarily focused on optimizing the proximity loss and selecting the appropriate classification loss. In setting A, we assessed the model with no proximity loss, defined as $\mathcal{L} = \mathcal{L}^{UD} + \gamma \cdot \mathcal{L}_{prox}(x, x^{\alpha})$, where $\gamma = 0$. Settings B1, B2, and B3 were evaluated with a proximity loss weighted by $\gamma \in \{0.1, 1.0, 10.0\}$. In the final configuration, C, based on B2, we replaced the mean square error classification loss with cross-entropy loss. For the CelebA dataset, we revisited settings A and B2 from the MNIST experiments. Setting A yielded the highest accuracy and lowest MSE (consistency), but the generated counterfactuals lacked coherence and showed no resemblance to the input data, as indicated by the high FID score. The FID played a crucial role in selecting setting B2, which includes the proximity loss.

AttFind [30]. As AttFind was not part of the main paper's comparative study, we applied it directly to our GdVAE's latent space without optimization. Refer to Tab. 15 for the results.

EBPE [43]. To evaluate EBPE, we experimented with different hyperparameters and activation functions in the decoder's output layer. The initial implementation, designed exclusively for CelebA, used the parameters detailed in Tab. 16 ("Original") as our starting configuration. However, this configuration yielded suboptimal performance on both MNIST and CelebA. For MNIST, setting A from Tab. 16 was chosen for its balance between consistency and realism.

EBPE encountered challenges in generating good reconstructions for the CelebA dataset with our backbone network and the original settings (see Tab. 16). To address this issue, we explored different activation functions to prevent image saturation, particularly as our GdVAE architecture employed a ReLU function in the output layer. In setting A, we employed a Sigmoid function, while method

Table 15: Evaluation of CF explanations for the simple consistency task. Methods marked with a † exclusively induce class changes, rendering accuracy incomparable to other methods. These † methods closely adhere to the original implementation. We use ACC to assess the classification consistency for generated CFs. The Fréchet Inception Distance (FID) is employed to gauge CF realism. Proximity is measured with MSE (scaled by 10^2). Mean values, with standard deviation, are reported across four training runs with different seeds. It is evident that all methods marked with † achieve 100% accuracy in altering the class of the query image. The methods without a † represent the modified versions discussed in the main paper. These methods enable users to pre-define a confidence value when generating CFs.

MNIST - Binary 0/1			
Method	Consistency	Realism (FID) ↓	Proximity
	$ACC\% \uparrow$	$\widehat{p}_c \in [0,1]$	$MSE \downarrow$
AttFind† [30]	100.0±0.0	120.14±21.88	11.92±6.69
C3LT† [26]	100.0±0.0	88.67±11.01	14.92±0.85
C3LT [26]	3.6±0.8	57.09±10.78	5.83±1.47
CelebA - Smiling			
Method	Consistency	Realism (FID) ↓	Proximity
	$ACC\% \uparrow$	$\widehat{p}_c \in [0,1]$	$MSE \downarrow$
AttFind† [30]	100.0±0.0	109.18±14.82	2.32±1.37
C3LT† [26]	100.0±0.0	171.72±7.97	8.59±0.84
C3LT [26]	11.8±5.5	101.46±11.56	3.97±0.86

B1 utilized a hyperbolic tangent (tanh) function—the latter being used in the original GAN model by the authors of EBPE. Hence, all subsequent settings adopted the tanh function in the decoder architecture. Emphasis was placed on optimizing the reconstruction quality and FID scores by varying the weight of the conditional GAN loss (discriminator loss). Specifically, settings B1, B2, and B3 utilized weights of $\lambda_{cGAN} \in \{0.01, 0.1, 0.001\}$ for the discriminator loss.

Building on these findings, we enhanced the FID of version B1 by employing a higher weight of $\lambda_{rec} = \lambda_{cyc} = 10^3$ for the reconstruction loss in setting C, deviating from the previously used weight of 10^2. To validate our implementation, we used EBPE to explain a separate discriminative classifier. The objective was to assess whether further improvements could be achieved by extending the training time beyond the 24 epochs that was used by all other methods, as the original implementation employed 300 epochs. Consequently, methods D1, D2, and D3 were executed with 24, 48, and 96 epochs, respectively. To expedite training, we employed a single discriminative classifier instead of the GdVAE, and as a result, standard deviations are not reported. It's evident that EBPE requires more training time compared to the GdVAE, and with four times the training duration, it converges toward similar FID values as our global method. The results of this hyperparameter analysis are shown in Tab. 12.

C3LT [26]. We examined two loss function settings on MNIST and CelebA. Setting A employs the mean squared error, as utilized by GANalyze (Eq. (27)), while setting B is founded on the cross-entropy loss for $\mathcal{L}_{cf}$. The results are summarized in Tab. 12.

Table 16: Hyperparameters for EBPE.

MNIST						
Setting	λ_{cGAN}	λ_{rec}	λ_{cyc}	λ_{cfCls}	λ_{recCls}	Activation
A	0.01	1	10	10	0.1	ReLU
CelebA						
Setting	λ_{cGAN}	λ_{rec}	λ_{cyc}	λ_{cfCls}	λ_{recCls}	Activation
Original	1	10^2	10^2	1	1	tanh
A	0.01	10^2	10^2	1	1	Sigmoid
B1	0.01	10^2	10^2	1	1	tanh
B2	0.1	10^2	10^2	1	1	tanh
B3	0.001	10^2	10^2	1	1	tanh
C	0.01	10^3	10^3	1	1	tanh

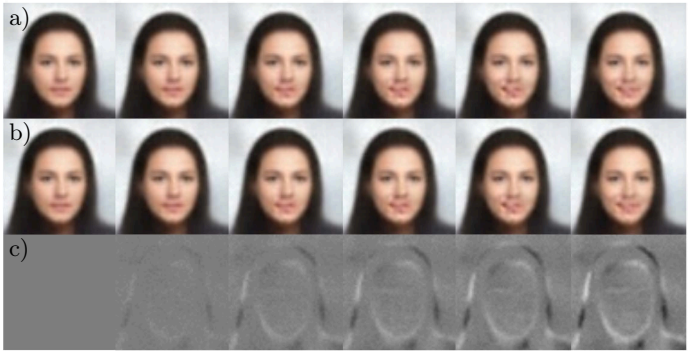

Fig. 11: a) Local-L2 CFs, b) Local-M CFs, and c) the difference, with white and black indicating a deviation of approximately ±3%.

E.3 Qualitative Results

Additional results: MNIST in Fig. 12, CelebA in Fig. 13, FFHQ in Fig. 14, and multi-class CFs for MNIST and CIFAR in Figs. 15 and 16. All local explanations were generated using the L2-based method. A comparison of local-L2 and local-M explanations is provided in Fig. 11.

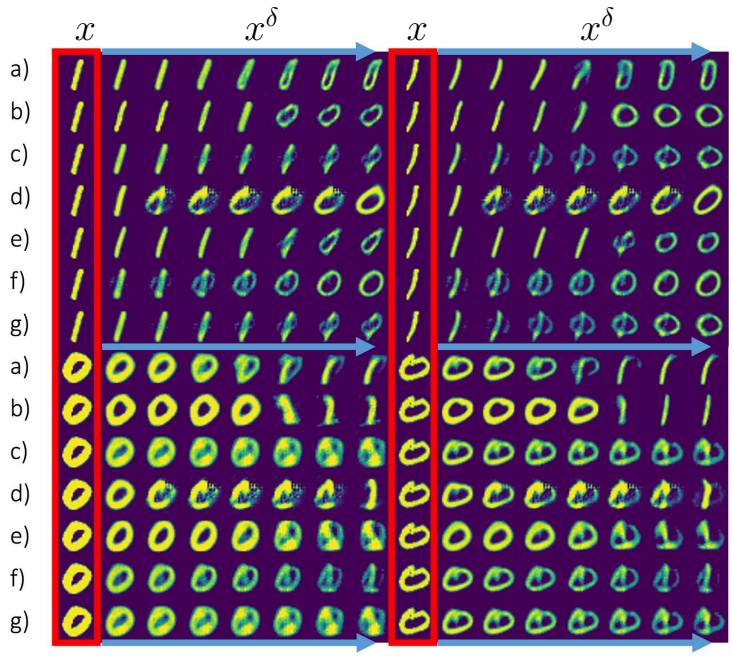

Fig. 12: MNIST CFs. We generate CFs (x^δ) linearly for the input, with decreasing confidence for the true class from left to right. On the leftmost side of each section, x denotes the input. We generate samples for $p_c = [0.99, 0.95.0.75, 0.5, 0.25, 0.05, 0.01]$. a) GANalyze, b) UDID, c) ECINN, d) EBPE, e) C3LT, f) Ours (global), g) Ours (local).

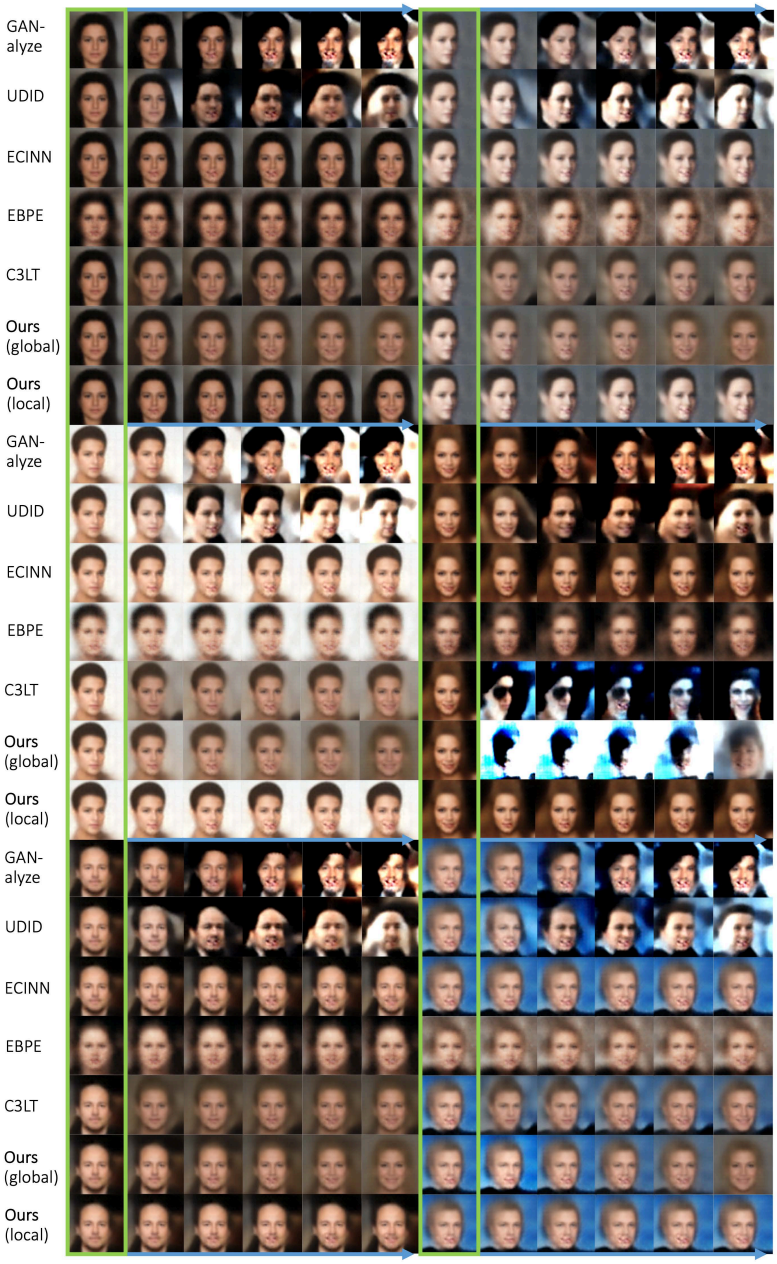

Fig. 13: CelebA CFs

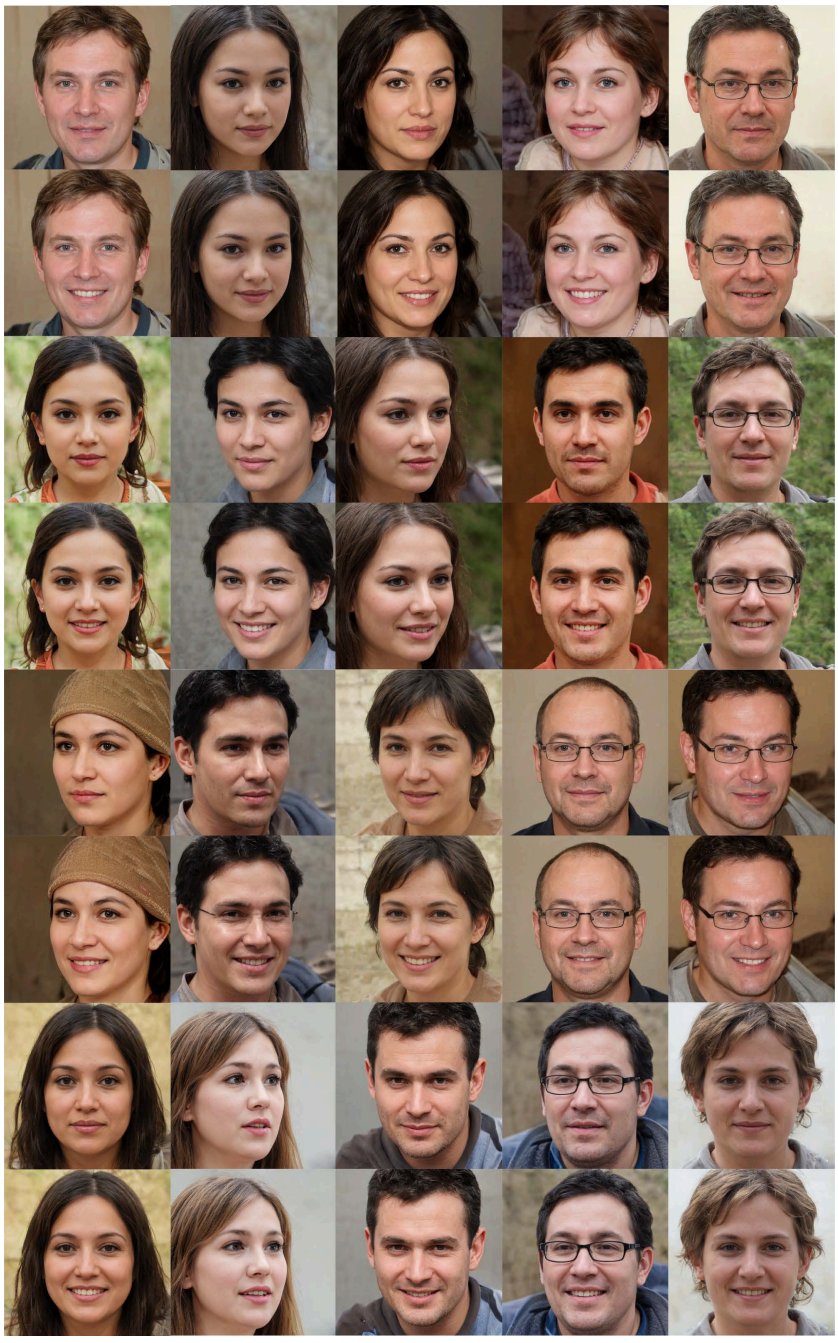

Fig. 14: FFHQ CFs

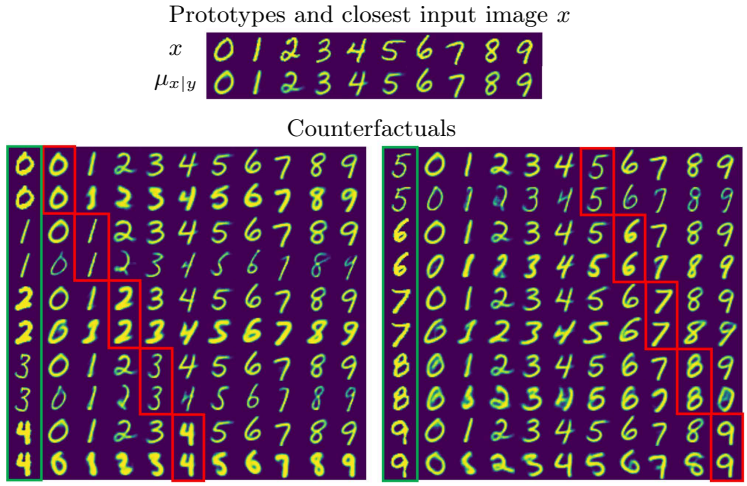

Fig. 15: MNIST multi-class CFs. CFs for the simpler consistency task by swapping the logits of the predicted and counterfactual classes. The green rectangle indicates the input image, while the red rectangles highlight the image reconstructions. Global (top) and local (bottom) CFs are each positioned to the left and right of the reconstructions, respectively. The local CFs maintain key image characteristics, such as line thickness. This CF strategy changes class predictions 100% of the time for the global method, and 99% of the time for the local method.

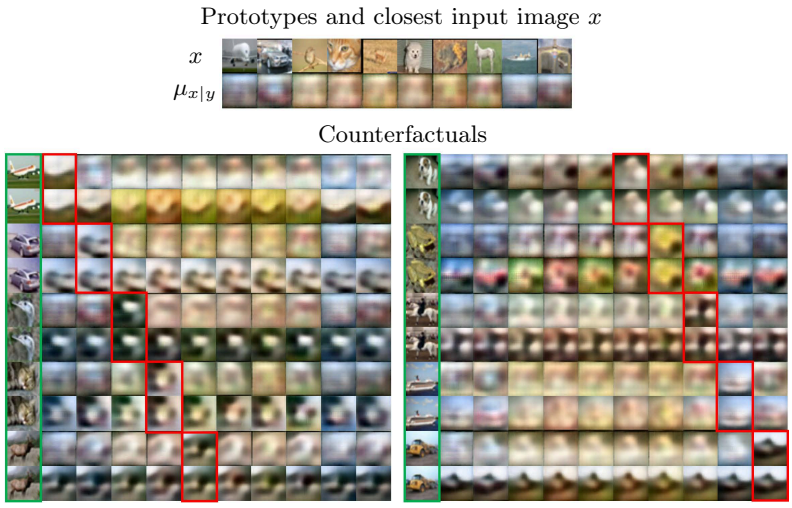

Fig. 16: CIFAR-10 multi-class CFs. CFs by swapping the logits of the predicted and counterfactual classes. The green rectangle indicates the input image, while the red rectangles highlight the image reconstructions. Global (top) and local (bottom) CFs are each positioned to the left and right of the reconstructions, respectively. The CFs are generated primarily through color adjustments and minor shape adaptations. This CF strategy changes class predictions 97% of the time for the global method, and 89% of the time for the local method.

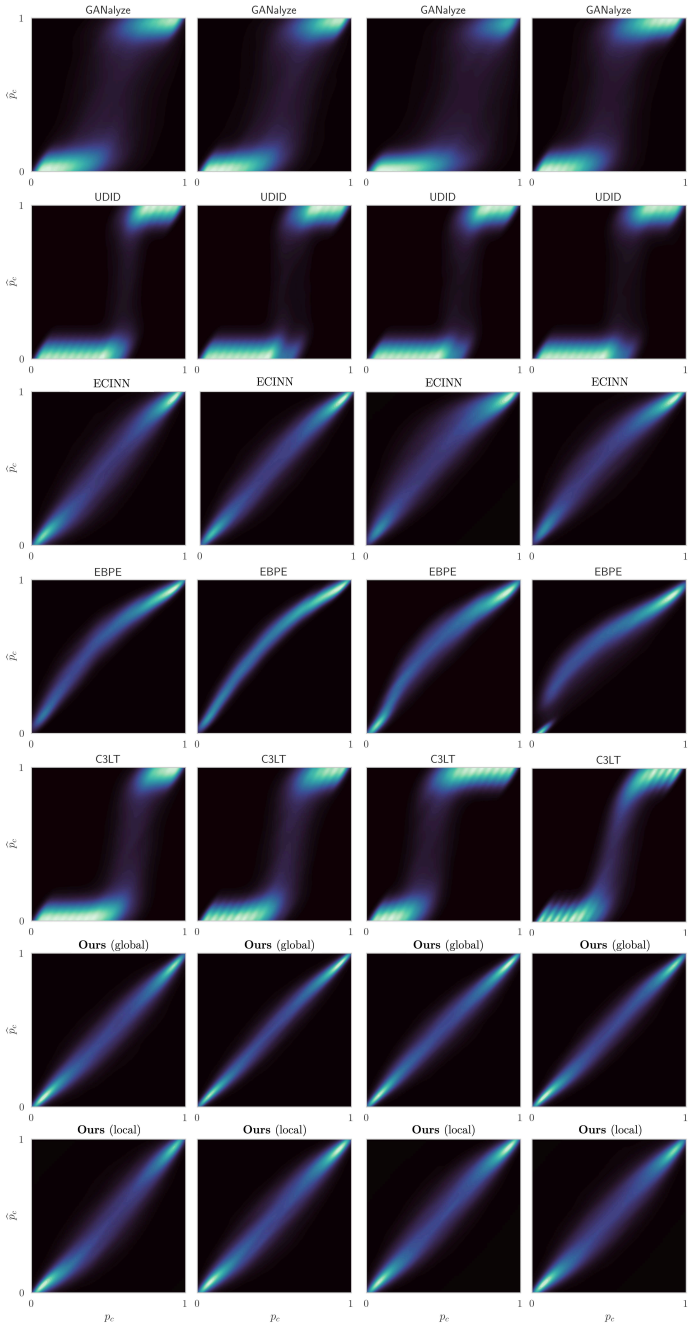

Fig. 17: MNIST KDE plots are employed to visually depict the relationship between the requested confidence value p_c and the predicted confidence by the classifier $\widehat{p}_c = p_\theta(y = c|h(g(z^\delta)))$ for the counterfactual $z^\delta = \mathcal{I}_f(z, \delta)$.